Geophysical Journal International

Geophys. J. Int. (2012) **190,** 1181–1196 doi: 10.1111/j.1365-246X.2012.05544.x

Seismic velocity structures in the southern California plate-boundary environment from double-difference tomography

A. A. Allam and Y. Ben-Zion

Department of Earth Sciences, University of Southern California, Los Angeles, CA 90089-0740, *E-mail: aallam@usc.edu*

Accepted 2012 May 10. Received 2012 May 10; in original form 2011 November 2

SUMMARY

We present tomographic images of crustal structures in the southern California plate-boundary area, with a focus on the San Jacinto fault zone (SJFZ), based on double-difference inversions of earthquake arrival times. Absolute arrival times of 247 472 *P* and 105 448 *S* wave phase picks for 5493 earthquakes recorded at 139 stations in southern California are used. Starting with a layered 1-D model, and continuing in later iterations with various updated initial models, we invert the data for V_p and V_s in a 270 km long, 105 km wide and 35 km deep volume around the SJFZ using a spatially variable grid with higher density around the SJFZ. The examined volume stretches from Cajon Pass to the northernmost Imperial Fault Zone and includes portions of the southern San Andreas Fault (SAF), the Elsinore Fault and the Brawley Seismic Zone in the Salton Trough. Because differential traveltimes used in the double-difference inversions are most sensitive to near-source structures, we obtain high resolution around the earthquake sources. After 30 iterations we improve the average traveltime misfit by a factor of 16. Though ray coverage is limited at shallow depths, we obtain detailed images of seismic velocities from 3 to 20 km throughout much of the study area. Our final velocity results show zones of low-velocity and anomalous V_p/V_s ratios associated with various fault strands and sedimentary basins, along with clear velocity contrasts across the SJFZ and the southern SAF. The velocity reductions in fault zone regions are generally highest in geometrically complex areas (up to 30–50 per cent in the top few kilometres), are higher for V_s than for V_p, and follow a flower-type pattern with depth. In the central section of the SJFZ, from the San Jacinto valley to the trifurcation area, the northeast side of the fault has generally higher seismic velocities than the southwest block. The obtained contrasts of V_p are more persistent and higher (up to 20 per cent) than the contrasts of V_s (up to 15 per cent), although the differences may stem (at least partially) from the higher resolution of V_p images. In the SJFZ sections to the northwest and southeast, there are patches with reversed velocities contrasts especially in the shallow crust near the San Jacinto Valley and other basins. Along the Banning fault there is no clear velocity contrast. For the southern SAF, the northeast side has generally lower seismic velocities in the seismogenic zone with patches of contrast reversals in the shallow crust. In the Brawley Seismic Zone, the northeast side has somewhat lower velocities in the ∼20 km section near the southern SAF and higher velocities farther to the southwest. The imaged features have important implications for various aspects of earthquake and crustal dynamics in the region.

Key words: Earthquake dynamics; Body waves; Seismic tomography; Transform faults; Continental margins: transform; Crustal structure.

1 INTRODUCTION

Fault zone structures can exert important controls on several aspects of earthquake ruptures, seismic radiation, inter- and post-seismic deformation and local seismicity patterns (e.g. Ben-Zion 2008 and references therein). As examples, Michael & Eberhart-Phillips (1991) suggested relations between endpoints and areas of high moment release of moderate to large earthquakes and seismic velocities around several fault zones in central and northern California. Eberhart-Phillips & Michael (1993), Thurber *et al*. (2006) and Zhao *et al*. (2010) discussed connections between the velocity structure at the Parkfield section of the San Andreas Fault (SAF) and earthquake behaviour in the region. Rubin & Gillard (2000), Zaliapin & Ben-Zion (2011) and Lengline & Got (2011)

found correlations between the degree of seismic velocity contrast across faults in California and directivity and along-strike symmetry properties of seismicity on the faults.

In this paper we use double-difference tomography (DDT; Zhang & Thurber 2003; Thurber *et al.* 2006) to image *P* and *S* seismic velocities in a crustal volume around the San Jacinto fault zone (SJFZ) in southern California that includes the southern SAF, Elsinore fault, Brawley Seismic Zone and northern Imperial fault. We focus on velocity contrast (bimaterial) interfaces and low-velocity fault zone materials. Prominent bimaterial interfaces can be relevant for propagation directions of earthquake ruptures (e.g. Weertman 1980; Shi & Ben-Zion 2006; Lengline & Got 2011), and affect the generation of frictional heat (e.g. Andrews & Ben-Zion 1997; Ben-Zion & Huang 2002), off-fault damage (e.g. Ben-Zion & Shi 2005; DeDontney *et al*. 2011), geodetic fields (e.g. Le Pichon *et al*. 2005; Wdowinski *et al*. 2007), seismic ground motion (e.g. Ben-Zion 2001; Brietzke *et al.* 2009) and spatial distribution of seismicity on the fault (e.g. Rubin & Gillard 2000; Zaliapin & Ben-Zion 2011). The extent and intensity of low-velocity fault zone rocks can provide information on the long-term organization of faults (e.g. Ben-Zion & Sammis 2003; Kim *et al.* 2004), governing brittle rock deformation (e.g. Lyakhovsky & Ben-Zion 2009; Doan & Billi 2011) and stress fields operating during earthquake ruptures (e.g. Andrews 2005; Ben-Zion & Shi 2005; Dunham *et al.* 2011). The existence of fault bimaterial interfaces and low-velocity zones can also affect routine derivations of earthquake locations and focal mechanisms (e.g. McNally & McEvilly 1977; Oppenheimer *et al.* 1988; Ben-Zion & Malin 1991).

1.1 Regional and geological setting

The complex boundary environment between the North American and Pacific plates in southern California, a roughly 200 km wide zone with various geological terranes, provides an excellent natural laboratory for studying the interaction of fault zone structures and earthquake properties. The total relative motion between the North American and Pacific plates in the area is about 50 mm yr^{-1} averaged over the past 3 Ma (DeMets 1995; DeMets & Dixon 1999). Geodetic studies show that the present-day motion of 45 mm yr^{-1} is divided equally between the southern SAF and the SJFZ, with a smaller component accommodated by the Elsinore fault (Fialko 2006). In the present work we image all three and additional faults, but the focus is on the structure of the SJFZ which is currently the most seismically active fault zone in southern California.

The SJFZ is a dominantly right-lateral fault zone that extends roughly 230 km southeast from the San Gabriel Mountains through the Salton Trough (Fig. 1). Approximately 24 km of slip has accumulated across the SJFZ since the latest Pliocene to early Pleistocene (Rockwell *et al*. 1990; Kirby et al. 2007), with estimated slip rates that vary along-strike between 8 and 20 mm yr^{-1} (Kendrick

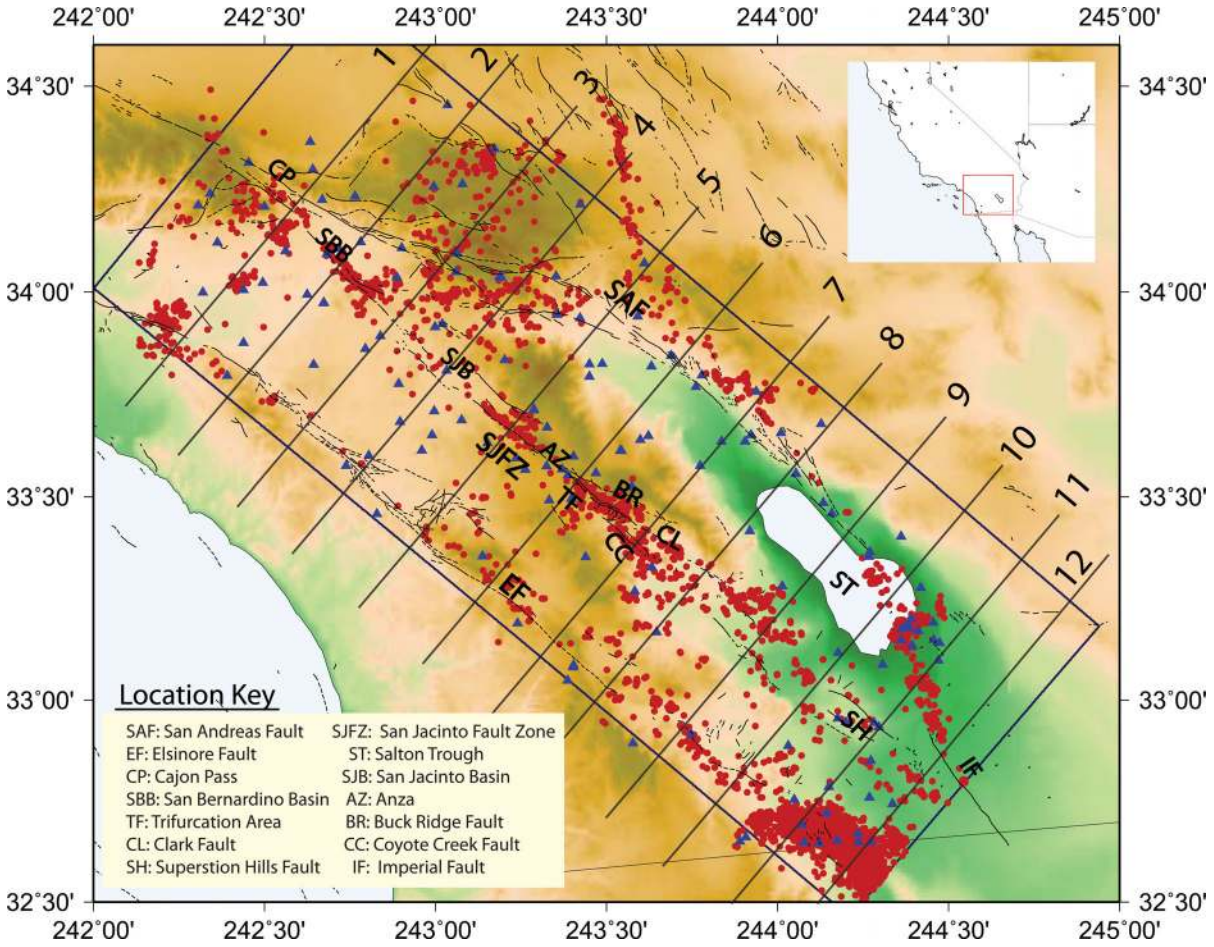

Figure 1. Location map for the San Jacinto fault zone (SJFZ) environment with 5493 $M_w > 2.2$ earthquakes from the SCEDC catalogue (red circles), seismic stations (blue triangles) and surface traces of large faults (black lines). The box outlines the region parametrized in the inversions for V_p and V_s seismic velocities. The background colours indicate topography with brown being high and green being low. Localities of interest are labelled as shown in the location key. Map view for different depth sections of the area are shown in Figs 4 and 5. Cross-sections of velocities along profiles 1–12 are shown in Figs 6 and 7.

et al. 2002; Rockwell 2003; Fay & Humphreys 2005; Fialko 2006). For comparison, the slip rates along the SAF vary between 10 and 35 mm yr^{-1}, with lower rates in southern California that are comparable to those of the SJFZ. The SJFZ is thought to have formed gradually over the past 1.5 Ma through transfer of slip from the less favourably oriented SAF segment in the Banning Pass (Langenheim *et al.* 2004). It consists of multiple segments at the surface, each exhibiting different geometrical and seismic properties, and is associated with diverse geological units and damage structures near the surface (e.g. Wechsler *et al.* 2009; Salisbury *et al*. 2011; Morton *et al*. 2012).

In the northern part, the SJFZ branches from the SAF at Banning Pass, an area with broadly distributed seismicity. The Anza segment in the central fault zone is generally referred to as the Anza Seismic Gap because of a lack of instrumentally recorded seismicity in the last few decades. This segment is well expressed geomorphically with localized slip zones and is thought to rupture in large events (Rockwell *et al.* 2006; Rockwell & Seitz 2008). Detailed geological mapping of rock damage in the Anza area documented considerable asymmetry across the fault, with most rock damage being on the northeast side (Dor *et al.* 2006). South of the Anza Gap, the SJFZ branches into three strands in a series of stepovers: the Clark, Buck Ridge and Coyote Creek faults. All three faults are seismically active, producing broad zones of seismicity in the restraining bend south of Anza. Seismological and geological observations in this area show zones of damaged rocks adjacent to the faults with higher damage intensity in general to the northeast (Lewis *et al*. 2005; Wechsler *et al.* 2009). Because of its large total displacement, the SJFZ juxtaposes various lithologies. In the northern fault zone, Pleistocene gravels are in contact with Cretaceous plutonic rocks (Sharp 1967). The northern SJFZ is also coincident with a compositional boundary between the western and eastern sections of the Peninsular Ranges batholith (e.g. Silver & Chappell 1988). The SJFZ may have exploited the compositional boundary when it branched from the SAF (Magistrale & Sanders 1995). Near Anza in the central part of the SJFZ, Quaternary marine sedimentary units are in contact with metamorphic rocks (Jennings 1977).

1.2 Related imaging studies

The juxtaposition of different lithologies and presence of damaged fault zone rocks create steep gradients in local seismic velocity that can produce fault zone head waves and/or trapped waves (e.g. Ben-Zion 1989, 1990; Ben-Zion & Aki 1990). Previous regional imaging studies found evidence for both a velocity contrast across the SJFZ and damage zones (Scott *et al*. 1994; Hauksson 2000; Hong & Menke 2006; Tape *et al*. 2009; Lin *et al.* 2010). However, these studies disagree on the width and depth of the damage zones and degree of velocity contrast. The disagreements can largely be explained by differences in data sets and resolution of the employed methods. In finite-frequency tomography the ultimate resolution is limited by the data coverage and employed frequency-range, whereas in traveltime tomography it is limited by the distribution of data and grid size.

The SJFZ-focused traveltime tomography by Scott *et al*. (1994) was parametrized at a uniform grid spacing of 5 km, which captured a velocity contrast but was insufficient to show low-velocity fault zone structures. Hong & Menke (2006) used noise-based imaging associated with cross-correlations among stacked seismic records (e.g. Shapiro *et al*. 2005) and observed fault damage zones in results spatially averaged over 5 km areas. Li & Vernon (2001), Lewis *et al*. (2005) and Yang & Zhu (2010) used seismic phases propagating within low-velocity fault zone layers and observed 100 m wide trapping structures in the trifurcation area of the SJFZ. These features are below the resolution of the regional imaging studies. A double-difference traveltime inversion by Lin *et al*. (2010) was performed on a uniform grid spacing of 10 km, which was sufficient only for the largest fault-related features. Tape *et al*. (2009) performed a regional finite-frequency tomography in the area with a grid spacing of 1 km. However, the study included smoothing of sensitivity kernels and used only 143 events from across southern California. The resolution of the final model was estimated to be ∼3 km vertically and ∼20 km horizontally (Tape *et al.* 2010).

In the present work, we perform a considerably more detailed imaging of the SJFZ area using double-difference traveltime tomography with high sensitivity to features of interest (i.e. bimaterial interfaces and damage zones) near the earthquake sources. Traditional resolution analysis tests suggest that the obtained results have a horizontal resolution of ∼5 km regionally (Appendix A) and ∼500 m within the SJFZ itself (Supporting Information; Fig. S2b).

2 ANALYSIS

2.1 DDT

We first review briefly the general formulation of DDT for completeness. Specific model parameters used in this work are discussed in Section 2.2. DDT is a seismic imaging method developed by Zhang & Thurber (2003) that takes the difference in body wave traveltime between nearby source pairs to cancel path effects and simultaneously invert for seismic velocity and hypocentre location. DDT is based on the double-difference hypocentre relocation algorithm of Waldhauser & Ellsworth (2000), which uses ray tracing to correct event locations by subtracting the ray path effects of nearby event pairs observed at a common station. DDT is highly sensitive to seismic velocity in the near-source region because the ray paths for nearby events are nearly identical, and thus cancel when subtracted, outside of the source region. As such, DDT has been effective at imaging low-velocity zones and sharp contrasts for synthetic data sets, the Hayward Fault (Zhang & Thurber 2003) and the Parkfield section of the SAF (Thurber *et al.* 2006).

The main aspects of the DDT formulation are as follows. For a single event i at location x recorded at station k, the difference r between the predicted arrival time and observed arrival time T is given by

$$r_k^i = \sum\nolimits_{l=1}^{3} \frac{\partial T_k^i}{\partial x_l^i} \Delta x_l^i + \Delta\tau^i + \int_i^k \delta u \, ds, \tag{1}$$

where τ^i is the origin time, u is the slowness field of either the P or S phase, x^i is the source location and ds is an element of path length. In classical body wave tomography, both x^i and τ^i are held constant and only changes in u are considered; this assumption is not used in DDT. Subtracting a similar equation to (1) for nearby event j yields

$$r_k^i - r_k^j = \sum\nolimits_{l=1}^{3} \frac{\partial T_k^i}{\partial x_l^i} \Delta x_l^i + \Delta\tau^i + \int_i^k \delta u \, ds - \sum\nolimits_{l=1}^{3} \frac{\partial T_k^j}{\partial x_l^j} \Delta x_l^j - \Delta\tau^j - \int_j^k \delta u \, ds. \tag{2}$$

If events i and j are sufficiently close that the ray paths can be considered nearly identical, (2) can be simplified to

$$dr_k^{ij} = r_k^i - r_k^j = \sum_{l=1}^{3} \frac{\partial T_k^i}{\partial x_l^i} \Delta x_l^i + \Delta\tau^i - \sum_{l=1}^{3} \frac{\partial T_k^j}{\partial x_l^j} \Delta x_l^j - \Delta\tau^j = (T_k^i - T_k^j)^{\text{obs}} - (T_k^i - T_k^j)^{\text{cal}}. \quad (3)$$

Expression (3) is the double-difference equation of Waldhauser & Ellsworth (2000). However, because the differenced ray paths still have sensitivity near the source region, (2) will more strictly simplify to

$$dr_k^{ij} = r_k^i - r_k^j = \sum_{l=1}^{3} \frac{\partial T_k^i}{\partial x_l^i} \Delta x_l^i + \Delta\tau^i - \sum_{l=1}^{3} \frac{\partial T_k^j}{\partial x_l^j} \Delta x_l^j - \Delta\tau^j + u(s^*), \quad (4)$$

where $u(s^*)$ is the slowness in the region near events i and j. Because seismic velocities outside of the region s^* are also of interest, eqs (1) and (4) are combined for all hypocentral pairs and for all stations into the system of linear equations

$$G\mathbf{m} = \mathbf{d}. \quad (5)$$

Here $\boldsymbol{G}$ is of size $M \times 5N$, with M and N being the numbers of double-difference observations and events, respectively, containing the partial derivatives from (2), $\mathbf{d}$ is the data vector containing the double differences from (4) as well as the absolute traveltime residuals from (1) and $\mathbf{m}$ is a vector of length $5N$ $(\Delta\boldsymbol{x}, \Delta\tau, \delta u)^T$ containing the changes in model parameters to be determined. This system is solved by the LSQR method (Paige & Saunders 1982).

The combination of the double-difference formulation with classical tomography can yield high-resolution results of local fault zone environments. By linking thousands of event pairs through a chain of near-neighbours, it is possible to gain accurate resolution in the source region itself in a relative sense. The inclusion of single-event traveltimes and full ray paths constrains velocities along the path outside the source regions. As these ray paths tend to avoid low-velocity zones, the two data sets are complimentary. However, there are several limitations to this method. First, because it is based on ray theory, only small perturbations to velocity are allowed. This can be overcome simply by iterating the inversion, using the resulting model from a previous step as the new starting model. Secondly, DDT makes use only of *P*- and *S*-wave traveltimes; it ignores traveltimes of other phases and data of the full waveforms, notably surface waves. An updated version of the DDT not used in this study includes head waves refracting along fault zone bimaterial interfaces (Bennington *et al.* 2011). Thirdly, because ray theory is a high-frequency approximation there is no sensitivity outside of the ray path, creating sampling problems at higher resolution. That is, the finer the employed grid size, the less each ray samples the volume, resulting in a more poorly constrained inversion. We mitigate the latter problem by using a variable grid size and a progressive weighting scheme to constrain regional velocities before resolving fine-scale structure in the source region.

2.2 Data set and model parameters

We use *P* and *S* wave arrival time data of 5493 events with $M_w > 2.2$ primarily from the SJFZ, the southern SAF and the Elsinore fault obtained from the Southern California Earthquake Data Center (Fig. 1). A total of 247 472 *P* and 105 448 *S* wave phase picks recorded at 139 stations are included in all iterations, with an average of 39 picks per event. Each phase pick is made by automated software and assigned a quality rating between 0.0 and 1.0 by an analyst; we discard picks with quality less than 0.3. From this data set, we compute 151 575 differential traveltimes for event pairs with hypocentres having a maximum separation of 2 km. During the inversion process 119 events were relocated above the surface and discarded.

We perform our inversions in a discretized model space of dimensions 270 km × 105 km × 35 km in a coordinate system rotated 40° counterclockwise to approximately fault-parallel (x) and fault-normal (y) axes. We begin by solving for *P*-wave velocities (V_p) and earthquake locations on a uniform 1 km-spaced grid using a smoothed 1-D starting model (Fig. 2a) derived from Helmberger *et al*. (1992). The obtained velocities and event locations are then used iteratively as initial values for inversions on a variable grid that is progressively reduced to a minimum spacing of 100 m in the 4.5 km region on each side (y direction) of the SJFZ. The grid cells in the x and z directions remain uniformly spaced at 1 km. A more detailed discussion of the inversion grid and MATLAB code for generating it are included in Appendix B; a geographical location map for the grid points used is shown in Fig. S1. The variable grid parametrization provides maximum resolution near the fault zone itself while maintaining computational efficiency and avoiding the ray coverage issues inherent in ray theory. By calculating derivative weight sum (DWS) values (discussed in Section 3.1) and performing checkerboard tests (Appendix A and Supporting Information), we show that the geometry of the employed sources and receivers supports such high-resolution near-fault grid spacing. We solve jointly for V_p, V_s and hypocentre locations using a starting value of 1.732 for the V_p/V_s ratio (Lin *et al.* 2010) which corresponds to a Poisson solid.

Following the methodology of Zhang & Thurber (2003), we apply a hierarchical weighting scheme to the absolute and differential data. In the first four iterations, the absolute data is weighted by a factor of 10 more than the differential data to establish the general velocity structure and event locations. Progressively over 30 iterations, we increase the weight on the differential data to provide more detail in the source regions and more precise event locations (Fig. 2c). At the 15th iteration, weighting is equal between the two data sets. At the 24th iteration, weighting is a factor of 10 in favour of the differential data. We continue six iterations at this weighting to provide stable results. This scheme delivers features not present in inversions using equal-weight or systematically skewed weights.

3 RESULTS

3.1 Evaluation of model results

Following previous DDT imaging studies (Zhang & Thurber 2003; Zhang *et al.* 2004; Lin *et al.* 2010), we evaluate the quality of our model results based on four criteria: (1) improvement of fit to the traveltime data, (2) calculation of the DWS, (3) plausibility of hypocentre relocations and (4) resolution estimated from synthetic tests.

Fig. 2 shows the arrival time residual distribution based on the starting and final models. The traveltime residual root-mean-square (rms) for the initial model is 1623 ms with a maximum misfit of 9250 ms (Fig. 2a), and the rms of the final model is 107 ms with a maximum misfit of 507 ms (Fig. 2b). This drastic reduction by a factor of almost 16 in the misfit rms reflects the unsuitability

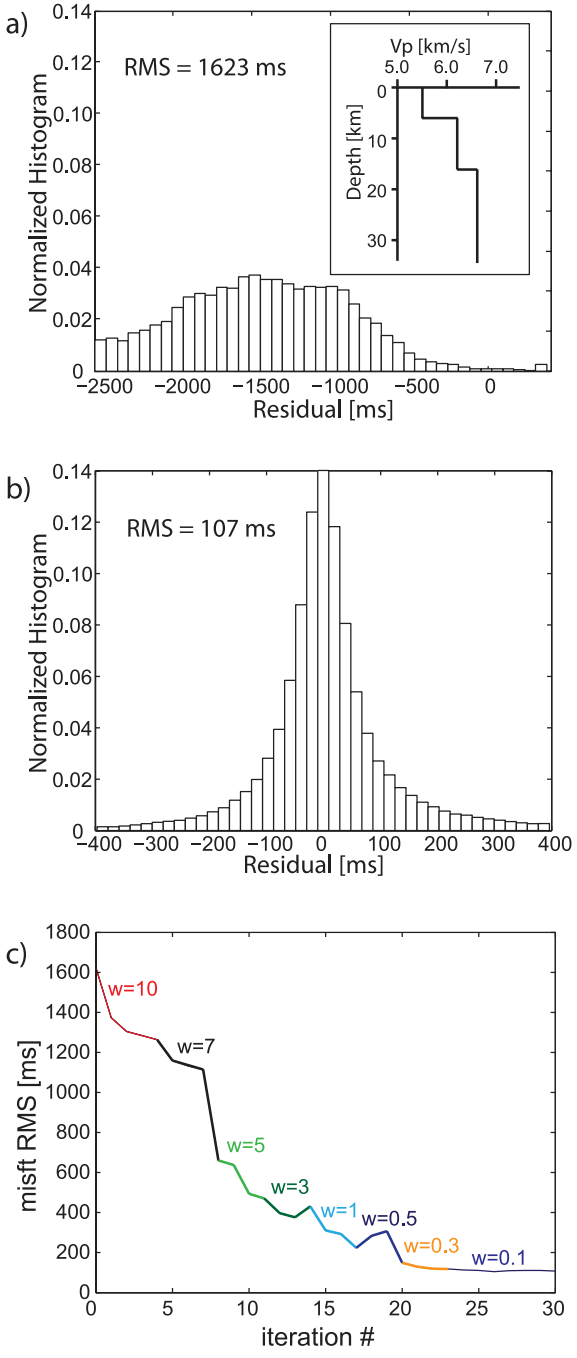

Figure 2. Histograms of traveltime residual ($T_{obs} - T_{calc}$) for 2 different models: (a) the initial 1-D model of Helmberger *et al*. (1992) and (b) the final model shown in Figs 4–9. The initial model features high residuals with a strong variance associated with a value of 1623 ms. The final model has a much improved rms of 107 ms and is associated with a highly peaked distribution. (c) Residual rms values of the output model after each inversion iteration and differential weight [w] between the absolute and relative traveltime data sets (colours). The initial improvement is rapid as the absolute traveltimes are given more weight. The jagged stair-step pattern is because of the weighting scheme; each step that changes the weight between absolute and differential traveltime data comes with a corresponding sharp reduction in misfit rms. The final six iterations have converged on a stable result.

of the initial 1-D model for predicting traveltimes and the inaccuracy of the initial hypocentre locations. In particular, the systematic negative bias introduced by the starting model is absent in the final model. Fig. 2(c) shows the residual rms for each iteration of the inversion. Most of the reduction occurs in the first few iterations because these iterations place the highest weight on the absolute traveltime. Most of the improvement from iterations 15–20 occurs in the differential traveltimes, which are most strongly affected by near-source velocity structure and hypocentre location. Changes in these parameters have less impact on the absolute traveltime misfit. The final six iterations produce little progressive improvement and converge on stable results. The quality of the final model may also be estimated by calculating synthetic waveforms based on the model and comparing the results to real data; however, this is beyond the scope of the present study.

The DWS is a useful measure of ray density at each model node (Thurber & Eberhart-Phillips 1999). The DWS for the lth model node is defined as

$$DWS_l = \sum_{i=1}^{N} \sum_{k=1}^{K} \frac{\partial T_{ik}}{\partial u_l}, \tag{6}$$

where N is the total number of events, K is the total number of stations and $\frac{\partial T_{ik}}{\partial u_l}$ is the change in traveltime with a change in slowness at node l. This last term is proportional to the ray path influenced by node l. By summing over all event-station pairs, the DWS reflects the total contribution of each node to the inversion. In this work, we plot contours for DWS values of 10 following Zhang *et al.* (2004). This value of DWS is based on the average DWS of all nodes compared to the total DWS of every node. Areas inside the contours are considered well sampled. Though somewhat *ad hoc,* the interpretation of our results is not very sensitive to the precise DWS threshold chosen as the local DWS gradients are quite steep.

Fig. 3 shows the initial catalogue hypocentre locations (blue) and the final relocated hypocentres (red). The average lateral change of events is 1.67 km, and the average change in depth is 2.36 km. These values are similar to those found in previous works with the DDT (Zhang & Thurber 2003). The gross pattern of relocations is consistent with the changes in velocities produced by progressive inversions. Events located in areas of lower than average velocities (e.g. the Salton Trough) are relocated towards the stations, whereas events in areas of higher average velocities (e.g. Banning Pass) are relocated further from the stations. Seismicity along the SFJZ and southern San Andreas is broadly distributed and does not collapse to well-defined fault planes after relocation. This is in contrast to other applications of DDT along the Hayward fault (Zhang & Thurber 2003) and Parkfield segment of the SAF (Bennington *et al.* 2011), but is in agreement with previous observations of seismicity patterns in the region (Hauksson 2000; Lin *et al.* 2007; Hauksson *et al.* 2012).

Appendix A discusses the effects of several inversion parameters and results of synthetic tests. The employed parameters are chosen to provide a balance between having too many unconstrained degrees of freedom and over-smoothing the results. As illustrated in Fig. A1 (see also Supporting Information), we are able to recover checkerboard-like models with (and without) a low-velocity fault zone layer and sharp velocity interfaces at high accuracy from 3 to 13 km depths. Fig. S2 (right) in the Supporting Information demonstrates that the performed inversions can detect and image (with some smearing) a 500 m wide fault zone. As noted previously, some care must be taken when interpreting the results of such tests (Lévêque *et al.* 1993); the tomographic resolution depends on the source–receiver ray paths, so an unrealistic model yields an unrealistic resolution. Specifically, ray paths tend to cluster around areas

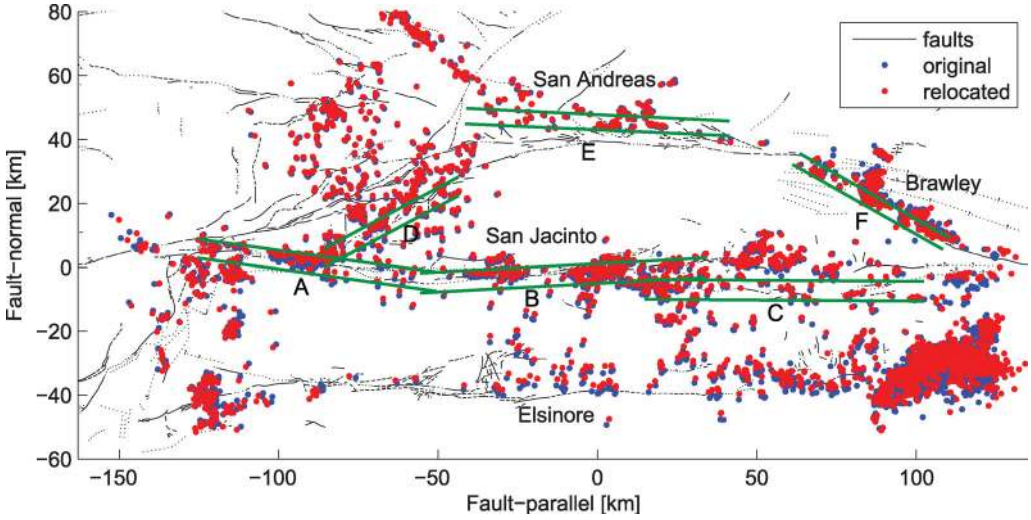

Figure 3. Initial (blue) and relocated (red) earthquake hypocentres. The systematic shifts of locations reflect the changes of seismic velocities across the faults. Velocity contrasts along profile pairs A–E chosen based on fault surface traces and seismicity patterns are shown in Fig. 8 (V_p) and Fig. 9 (V_s).

of high velocity and avoid areas of low velocity in the checkerboard models. As the true earth structure bears very little resemblance to checkerboard models, the resolution obtained from these tests is only a rough estimate. Nevertheless, both high- and low-velocity anomalies are recovered at seismogenic depths in the checkerboard tests shown in Appendix A and the Supporting Information. These synthetic results give us confidence in interpreting features of our velocity models in regions with DWS $\geq$ 10 for the plate-boundary region in southern California presented in the next section.

3.2 Tomographic images for the SJFZ and surrounding area

Figs 4 and 5 show, respectively, map views of V_p and V_s for the obtained tomographic results at various depths. The white contours enclose areas where the DWS values are above 10. The Elsinore fault is at the edge of the model and is poorly resolved for both V_p and V_s. We therefore exclude it from detailed discussion. At the regional scale, several expected geological features are expressed clearly in the tomographic images. The Salton Trough, a sediment-filled graben adjacent to the southern SAF (Jennings & Thompson 1986), is expressed as a low-velocity zone to roughly 7 km depth. Below this depth, velocities are higher than average in the Salton Trough, a feature expected because of crustal thinning in a region of extension. In addition, we observe several kilometres wide low-velocity zones along the SJFZ that are pronounced in the top 5 km and extend in stepover regions to about 8 km. The low-velocity zones are more pronounced for V_s than V_p. Northwest of the Salton Trough, we observe a velocity contrast along the SAF with the northeast side having overall lower seismic velocities. Along the SJFZ, there are regions with clear velocity contrasts at seismogenic depths. In the central section between the trifurcation area and the San Jacinto basin, the northeast side has higher seismic velocities. We also observe in the central section an asymmetric 6 km wide low-velocity zone that is primarily northeast of the fault. To the northwest, the presence of the San Bernardino and San Jacinto basins leads to a reversal in the velocity contrast polarity with lower velocities on the northeast side. Southeast of the trifurcation area, the low-velocity zone broadens and decreases in amplitude, while the velocity contrast continues along the Clark segment. As the SJFZ extends southeast into the Salton Trough, the contrast and low-velocity zones become indistinguishable from the basin structure. Some of the discussed features are shown more clearly in the fault-normal and fault-parallel cross-section views presented in Figs 6–9.

Figs 6 and 7 display, respectively, images of V_p and V_s on vertical planes along cross-sections 1–12 of Fig. 1. In profiles 1–4, the geometrically complex region between the SJFZ and SAF has low velocity. Profiles 2–4 show velocity contrasts along the SJFZ associated with the San Bernardino and San Jacinto basins. A comparison of profiles 4 and 5 shows that the polarity of the velocity contrast reverses from southwest fast in profile 4 to northeast fast in profile 5. Strong low-velocity zones with widths of about 6 km are apparent around the SJFZ between the San Jacinto Basin and trifurcation area (profiles 5–6). The low-velocity zones have up to 40 per cent reduction of V_s in the top 5 km or so of the crust and are surrounded by 'halos' of lower velocity reductions. These zones also narrow with depth, exhibiting flower structures that are primarily to the northeast of the fault. As indicated by the white contours, the imaging resolution is high in the general depth range of 3–16 km, so the depth variations of the low-velocity zones reflect genuine features of the fault zone structure. South of the trifurcation (cross-sections 7 and 8), we observe broad low-velocity zones around the SJFZ. Profiles 9–11 are dominated by the low velocity of the Salton Trough, whose southern boundary is sharply vertical, perhaps associated with the Superstition Hills fault. We do not observe in any cross-section clear low-velocity zones around the southern SAF, though the merging of the SAF with the Salton Trough would likely mask such a signal.

Figs 8 and 9 present results on the contrasts of V_p and V_s along the profile pairs A–F of Fig. 3. Each panel shown is the velocity of the northeast profile divided by the velocity of the southwest profile. The profile locations were chosen based on fault trace geometry, seismicity pattern and DWS resolution. White contours are for the minimum value of the DWS between the two profiles. Profile A is along the northwest SJFZ, from the intersection of SJFZ and the SAF to the San Jacinto Basin, and shows overall lower velocities to the northeast with variations along-strike and depth. Along profile B in the central section of the SJFZ, the velocity contrast reverses polarity and the northeast side has persistent faster velocities. This profile displays the highest contrast in velocity (about 20 per cent) near the Anza area. Profile C along the Coyote Creek

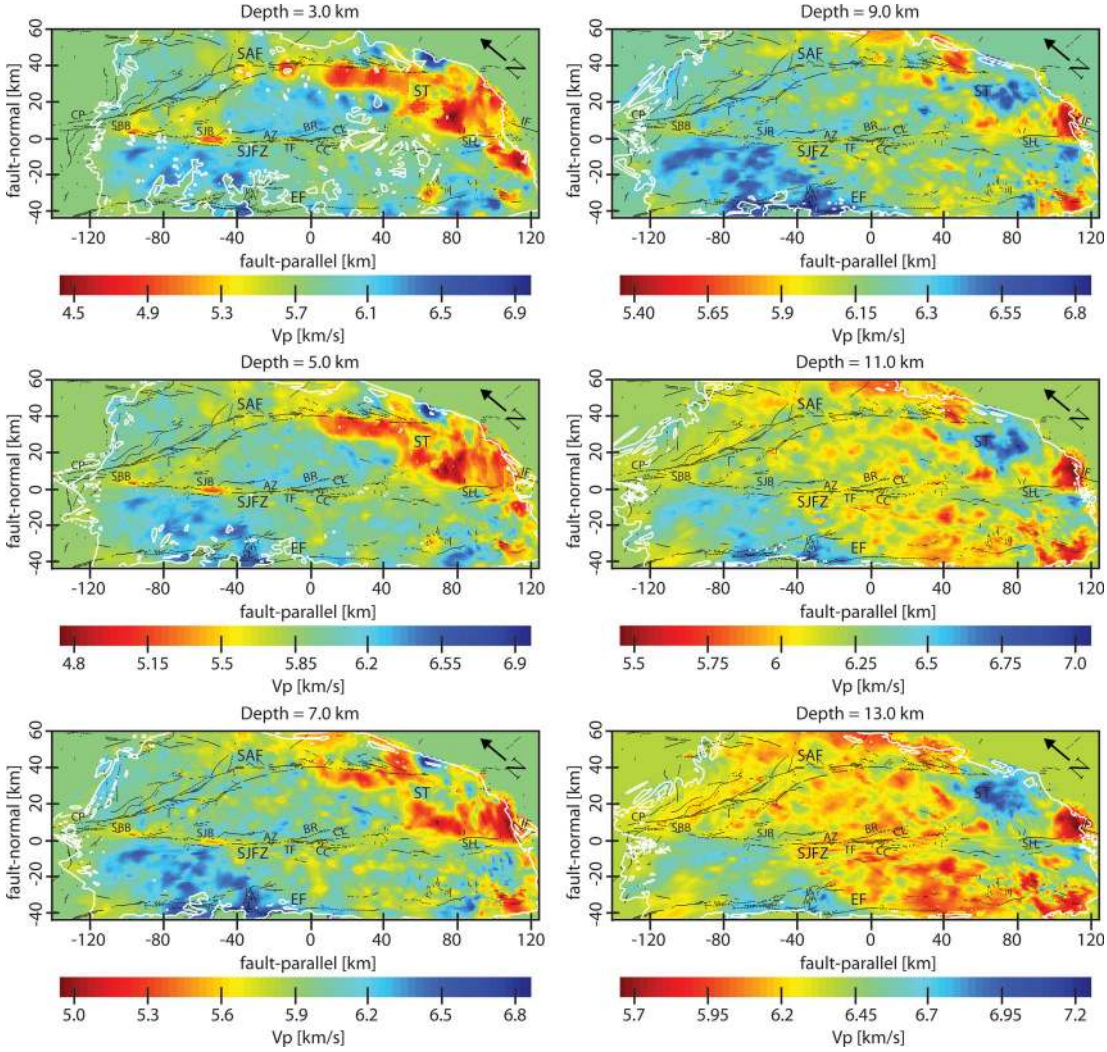

Figure 4. Map views of *Vp* at various depths for the box area in Fig. 1. The white contours enclose areas that are well sampled by the employed sources and receivers (DWS > 10). Localities of interest referred to in the text are labelled as indicated in the location key (shown in Fig. 1). The velocity scale is variable for increased visual resolution. The lowest velocity is observed in the rifted Salton Trough. Velocity contrasts are clear across both the SJFZ and SAF, though the polarity of these contrasts change along strike and with depth. In the northernmost SJFZ, the southwest side of the fault has higher velocities due to the San Bernardino and San Jacinto basins. Just southeast of the San Jacinto Basin, this contrast is reversed, with the northeast side of the fault zone having higher velocities through the end of the CL segment (see also Figs 8, profile B and 9, profile B). Low-velocity zones of varying degrees are associated with various strands of the faults (see also Figs 6 and 7). In the SJFZ, the strongest reductions of fault zone velocities are observed for the SJB and TF. In the geometrically simple Anza section, the velocity reduction is lowest.

and Superstition Hills segments, has minor contrast with a slightly faster northeast side and significant variations. Profile D along the Banning fault shows no overall contrast. Profile E along the Southern SAF is associated with a segment that is generally thought to dip to the northeast at ∼70° based on the seismicity and geodetic strain profiles (Richards-Dinger & Shearer 2000; Fialko 2006). The northeast side is overall slower at seismogenic depth, with a shallow reversal near the Salton Trough. Profile F along the Brawley Seismic Zone shows a spatially variable contrast in velocity, though resolution is poor in this region.

Because the velocity models obtained for V_s and V_p are of different resolutions, the images obtained by computing V_p/V_s values are noisy and contain numerical artefacts. The number of *S* wave phase picks is only ∼30 per cent of the total data set, so the resolution is lower for V_s than V_p, as shown in Appendix A. This numerical noise, with scale length of ∼5 km, is present even in synthetic tests where the V_p/V_s ratio of the 'true' model is held constant (Fig. S3). Nevertheless, there are interesting and persistent features observable in V_p/V_s, which we present in the Supporting Information (Figs S4 and S5). The central part of the SJFZ appears to be associated with a tabular zone with high V_p/V_s that is present primarily to the northeast of the fault and is seen to 9 km depth or more. The Salton Trough exhibits overall low V_p/V_s at shallow depths and high V_p/V_s below about 9 km. The San Jacinto Basin features low V_p/V_s at 3 km depth. Just northeast of the San Bernardino and San Jacinto basins there are localized zones with high V_p/V_s to 9 km depth. The regions between the SJFZ and the SAF to the northeast and Elsinore fault to the southwest are associated overall with moderate to low V_p/V_s.

4 DISCUSSION

The tomographic images obtained in this study provide the most detailed results on V_p and V_s currently available for the SJFZ environment. The derived velocity models contain important information

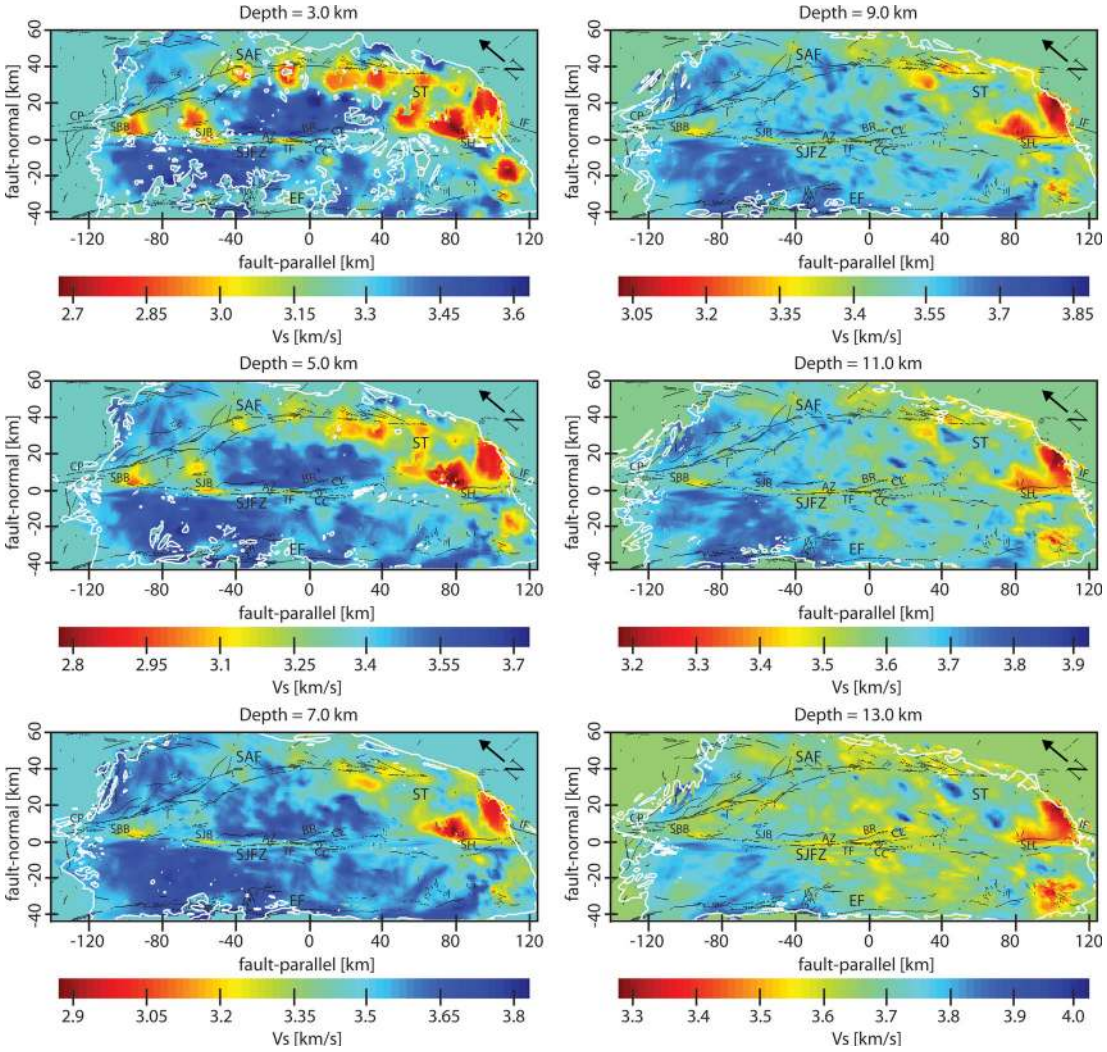

Figure 5. Similar to Fig. 4 for V_s values. The low-velocity zones are more pronounced for V_s than for V_p, with very strong reductions along the SJFZ to the northwest of the TF. See Figs 7 and 8 for additional details.

on low-velocity fault zone structures and bimaterial interfaces. These features reflect both past evolutionary processes and likely behaviour of future earthquakes in various fault zone sections. Our results are in general agreement with previous tomographic studies in places where the different images overlap, and the salient differences can be attributed to differences in data sets, resolution and methodology. Scott *et al*. (1994) showed a velocity contrast as high as 25 per cent across the Anza section of the SJFZ, but with a grid spacing of 5 km were unable to capture a low-velocity zone. The models of Magistrale & Sanders (1995), Hauksson (2000), Tape *et al*. (2009) and Lin *et al*. (2010) based on regional scale inversions do not capture the localized structure of the SJFZ, though broad-wavelength contrasts and low-velocity zones are observed in these studies. Such regional studies are the basis for the Southern California Earthquake Center community velocity models CVM-4 and CVM-H (Magistrale *et al.* 2000; Süss & Shaw 2003; Plesch *et al.* 2011) in the vicinity of the SJFZ.

The results of Figs 4–9 show clearly that the SJFZ is associated with a 3–6 km wide zone of low seismic velocity. These features are especially pronounced in the top 5 km or so of the crust and become narrower with depth exhibiting an overall flower-type structure. Near the trifurcation area, the significant broad low-velocity zone extends to a depth of about 7 km and obtains a maximum velocity reduction of 40 per cent. In the northernmost SJFZ, the low-velocity zone is indistinguishable from the low seismic velocities of the San Bernardino and San Jacinto basins. Previous work on these basins suggests that they are likely shallow features restricted to the upper 2 km (Graves 2008; Plesch *et al.* 2011). If so, the deeper low-velocity zones seen in these areas could be attributed to fault-related damage. To the south of the trifurcation area, the low-velocity zone is smeared across multiple segments and reduced in amplitude. Similar broad low-velocity zones around faults have been observed with gravity surveys (e.g. Stierman 1984), electromagnetic studies (e.g. Unsworth *et al.* 1999), geodetic data (e.g. Fialko 2004), seismic anisotropy (e.g. Cochran *et al.* 2003; Peng & Ben-Zion 2004) and noise-based imaging (Hong & Menke 2006).

The kilometres-wide damage zones are generally relic structures associated with the geological organization of the fault (e.g. Ben-Zion & Sammis 2003 and references therein). More intense and localized low-velocity zones that act as trapping structures (waveguides) for seismic waves are only about 100 m wide. Li & Vernon (2001) suggested that trapping structures extend in the

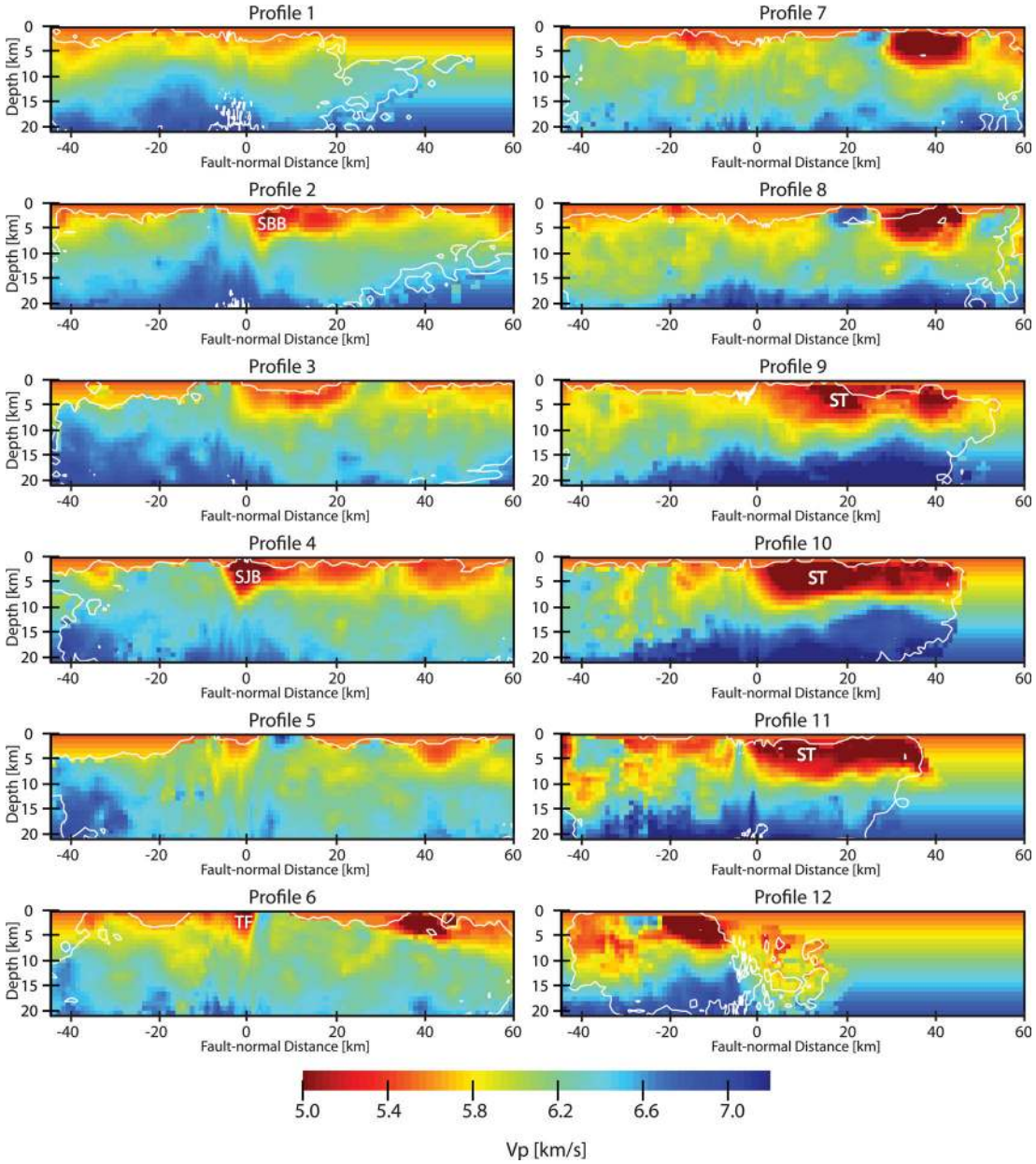

Figure 6. Fault-normal cross-section views of *Vp* at profiles 1 through 12 shown in Fig. 1. White contours enclose areas that are well sampled by the sources and receivers. Profiles 2–4 show broad low-velocity zones associated with the San Bernardino and San Jacinto basins, as well as the associated across-fault contrast with the relatively higher velocity material on the southwest side of the SJFZ. Profiles 5 and 6 show a reversal of this contrast and hallows of mild low-velocity zones extending to depths of 12–15 km. Profiles 7 and 8 show contrast across the SAF with higher velocities on the southwest side. Profiles 9–11 are dominated by the low-velocity Salton Trough in the upper 7 km, below which is a sharp gradient into a high-velocity region.

trifurcation area to a depth of 18 km, while Lewis *et al.* (2005) and Yang & Zhu (2010) concluded that the waveguides are limited to the top 3–5 km of the crust. The imaging of trapping structures is below the resolution of our study and other tomographic inversions. However, the flower-type shape with depth and strong variability of the imaged low velocity damage zones are consistent overall with results based on analyses of trapped waves and anisotropy using large data sets. Seismic trapping structures in the SJFZ (Lewis *et al*. 2005; Yang & Zhu 2010) and other locations exist typically only in the upper few kilometres of the crust and exhibit strong variations along-strike (e.g. Rovelli *et al*. 2002; Ben-Zion *et al*. 2003; Peng *et al*. 2003; Lewis & Ben-Zion 2010; Yang *et al*. 2011). Similar inferences have been made based on analysis of fault zone-related anisotropy and waveforms generated by repeating earthquakes (e.g. Peng & Ben-Zion 2004; Boness & Zoback 2006; Zhao & Peng 2009).

The observed flower structure shape of low-velocity zones with significant velocity reductions in the shallow crust are also consistent with numerical simulations of yielding regions around localized faults (e.g. Ben-Zion & Shi 2005; Ma & Andrews 2010). Near locations with significant geometrical heterogeneities that produce ongoing stress concentrations, slivers of rock damage can extend to the bottom of the seismogenic zone (e.g. Finzi *et al*. 2009). The diffuse halo of low damage in various places below the strong velocity reductions in the shallow crust likely reflects the increasing effectiveness of rock healing at depth because of increasing pressure and

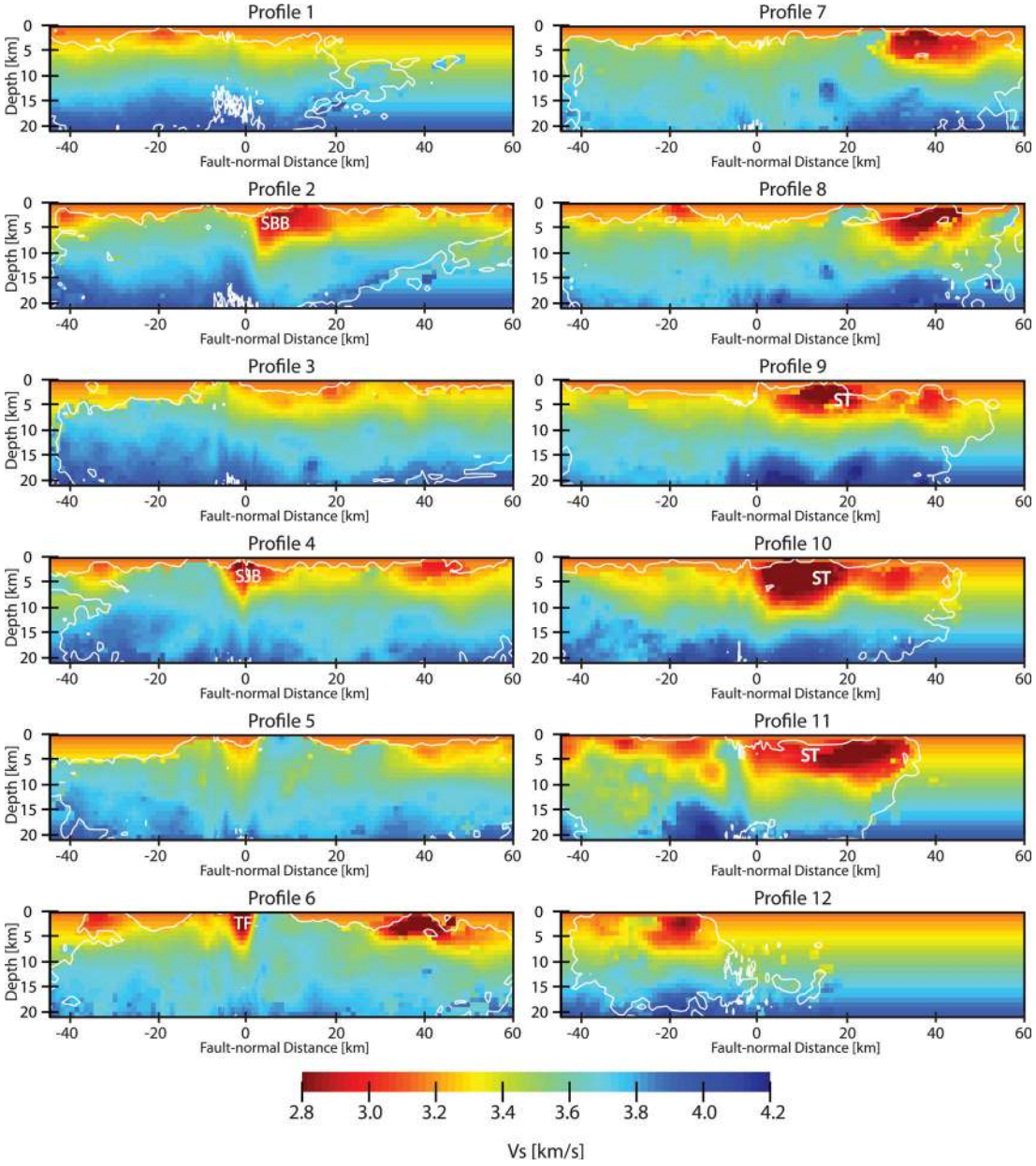

Figure 7. Similar to Fig. 6 for *Vs* values. The general features are similar as for *Vp*, though the low-velocity zones in profiles 5 and 6 are more pronounced in V_s. The resolvable area is slightly reduced because fewer *S*-wave traveltimes were available for use in the inversion.

temperature (e.g. Dieterich & Kilgore 1994; Johnson & Jia 2005; Lyakhovsky *et al.* 2011).

The tomographic images show clear contrasts of V_p and V_s across the central SJFZ, with the northeast block generally having higher seismic velocities (up to 20 per cent V_p contrast in the Anza gap area). Theoretical results for bimaterial ruptures (e.g. Ben-Zion 2001; Shi & Ben-Zion 2006; Ampuero & Ben-Zion 2008) predict a statistically preferred propagation direction of earthquake ruptures to the northwest in such a case. This is consistent with the observed across-fault asymmetry of rock damage mentioned in Section 3 (see Figs 4–7), the smaller scale asymmetry near Hog Lake (Dor *et al*. 2006) and the trifurcation area (Lewis *et al*. 2005; Wechsler *et al*. 2009; Yang & Zhu 2010), along-strike asymmetry of aftershocks (Zaliapin & Ben-Zion 2011) and generation of small-scale transpressive structures on one side of larger pull-apart basins (Ben-Zion *et al* 2012). We note that the central SJFZ, especially the area associated with the Anza gap, has the largest inferred slip for the past several large earthquakes (Salisbury *et al.* 2011). The observed overall reduction in the degree of velocity contrast with depth is consistent with high-resolution imaging based on *P* head and body waves along the creeping section of the SAF (Ben-Zion *et al*. 1992; Lewis *et al*. 2007; Zhao *et al*. 2010). This has a simple explanation in terms of a stronger effect of increasing normal stress on the lower velocity block that has higher density of cracks and other defects.

The smaller and less persistent velocity contrast in the trifurcation area and polarity reversal northwest of the San Jacinto Basin can act as dynamic barriers for ruptures attempting to propagate from the central SJFZ to the southeast and northwest (because of increasing normal stress at the propagating tip). On the other hand, earthquakes nucleating in the trifurcation area (or farther to the south) and propagating to the northwest will encounter dynamic

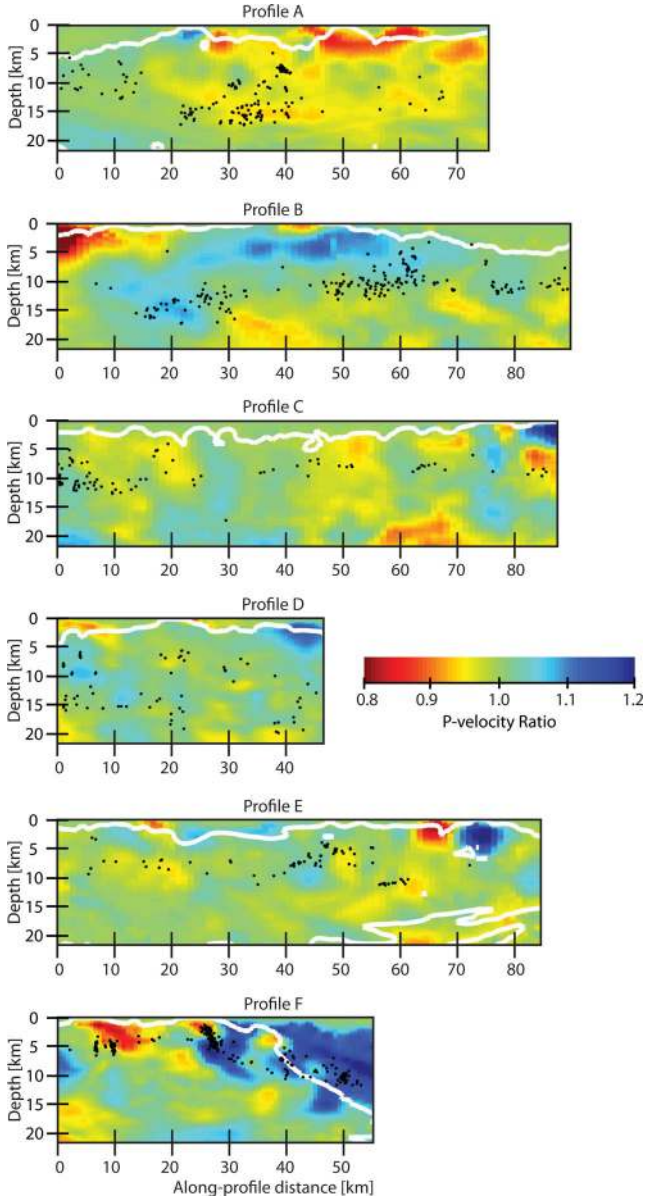

Figure 8. Cross-section views of V_p velocity ratio between profile pairs A–F shown in Fig. 3. Each panel is the V_p image of the northeast profile divided by the V_p image of the southwest profile. Blue colours indicate that the northeast profile has a higher velocity and red colours indicate the opposite. Profiles A–C are along the SJFZ, while profiles D–F are along the Banning fault, southern SAF and the Brawley Seismic Zone. Profile A along the northwest section of the SJFZ shows strong contrast in the top few kilometres associated with low velocities northeast of the fault near the San Bernardino and San Jacinto basins. Profile B shows a persistent contrast with higher velocity on the northeast side along the Anza and Clark segments, with a continuous and high amplitude contrast for 40 km along the Anza segment. Profile C along the Coyote Creek and Superstition Hills segments of the SJF and profile D along the Banning fault do not show clear persistent contrast. Profile E shows a slightly faster southwest side with shallow reversal near the Salton Trough. Profile F along the Brawley Seismic Zone shows alternating regions although resolution is poor in this area.

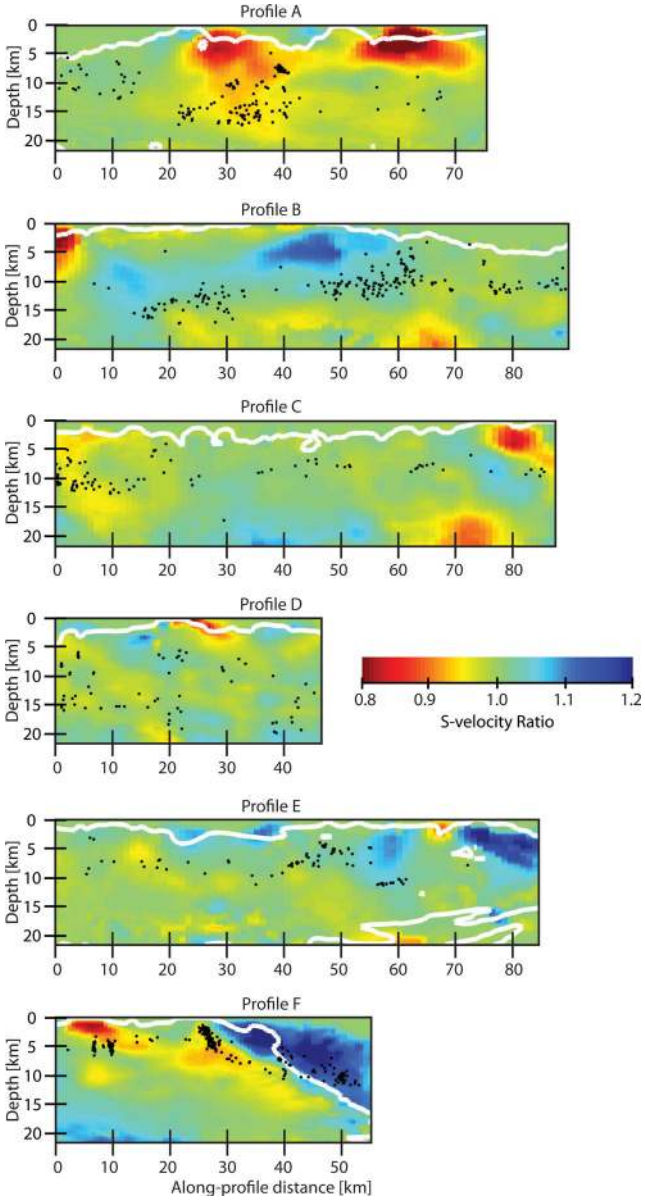

Figure 9. Similar to Fig. 8 for V_s values. The overall observed features correspond well to those shown for V_p in Fig. 8.

reduction of normal stress as they enter the Anza area and are likely to continue to propagate (with increasing slip) all the way to the San Jacinto Basin. More accurate velocity contrast images may be obtained in future studies using head waves that refract along fault bimaterial interfaces (e.g. Ben-Zion & Malin 1991; Hough *et al.* 1994; McGuire & Ben-Zion 2005; Bennington *et al.* 2011).

The obtained velocity structures also correlate well with geology and seismicity patterns. Regions of distributed seismicity feature broad zones of low seismic velocities, as in the Brawley Seismic Zone, east of the trifurcation area and northeast of the San Bernardino and San Jacinto basins. Regions of more focused ongoing seismicity, as in the Hemet stepover and trifurcation area, feature clear zones of highly reduced seismic velocity. Off-fault areas which lack seismicity have correspondingly high seismic velocity. These regions of high seismic velocity away from the fault zones correlate to first-order with surface geology. To the northeast of Anza, between the SJFZ and the SAF, a broad region of high

V_p and V_s corresponds to the intrusive igneous and metamorphic rocks observed at the surface (Sharp 1967). To the southwest of the San Bernardino Basin, a similar terrane dominated by plutonic rocks corresponds to a large region of relatively homogeneous high velocity. These two regions appear to be offset right-laterally across the SJFZ (Figs 4–5), though the apparent offset, on the order of 80 km, is much greater than the total 24 km of slip accommodated by the current SJFZ.

The model grid used in this work was designed to provide the highest resolution results with the employed method and data for the SJFZ environment. It would be useful to perform similar high-resolution imaging studies focusing on the regions around the southern SAF and the Elsinore fault. Detailed imaging of the Elsinore fault will probably require using either noise-based (e.g. Shapiro *et al.* 2005; Roux *et al.* 2011) or active-source (e.g. Bleibinhaus et al. 2007) techniques, given the scarcity of seismicity southwest of the fault. Future studies of the SJFZ using full waveform or adjoint tomography techniques (e.g. Chen *et al.* 2007; Tape *et al.* 2009) that incorporate fault zone head and trapped waves should be able to resolve more detailed fault zone features. As these methods involve comparison of modelled waveforms to real data, they require a reasonably accurate starting model. In particular, the initial model should include bimaterial interfaces and low-velocity zones at relevant places to produce fault zone head and trapped waves at appropriate sets of seismometers. The results of the present work contain these and other features, so they provide a good starting platform for more detailed future imaging studies.

ACKNOWLEDGMENTS

We are grateful to Haijiang Zhang for providing the DDT code and Cliff Thurber for many helpful discussions. The data used in this work are archived and distributed by the southern California Earthquake Data Center. The paper benefited from useful comments by Carl Tape and Haijiang Zhang. The study was supported by the National Science Foundation (grant EAR-0908903).

REFERENCES

Ampuero, J.-P. & Ben-Zion, Y., 2008. Cracks, pulses and macroscopic asymmetry of dynamic rupture on a bimaterial interface with velocity-weakening friction, *Geophys. J. Int.,* **173,** 674–692, doi:10.1111/j.1365-246X.2008.03736.x.

Andrews, D.J. & Ben-Zion, Y., 1997. Wrinkle-like slip pulse on a fault between different materials, *J. geophys. Res.,* **102,** 553–571.

Andrews, D.J., 2005. Rupture dynamics with energy loss outside the slip zone, *J. geophys. Res,* **110,** 1307–1321, doi:10.1029/2004JB003191.

Ben-Zion, Y., 1989. The response of two joined quarter spaces to SH line sources located at the material discontinuity interface, *Geophys. J. Int.,* **98,** 213–222.

Ben-Zion, Y., 1990. The response of two half spaces to point dislocations at the material interface, *Geophys. J. Int.,* **101,** 507–528.

Ben-Zion, Y., 2001. Dynamic rupture in recent models of earthquake faults, *J. Mech. Phys. Solids,* **49,** 2209–2244.

Ben-Zion, Y., 2008. Collective behavior of earthquakes and faults: continuum-discrete transitions, evolutionary changes and corresponding dynamic regimes, *Rev. Geophys.,* **46,** RG4006, doi:10.1029/2008RG000260.

Ben-Zion, Y. & Aki, K., 1990. Seismic radiation from an SH line source in a laterally heterogeneous planar fault zone, *Bull. seism. Soc. Am.,* **80,** 971–994.

Ben-Zion, Y. & Huang, Y., 2002. Dynamic rupture on an interface between a compliant fault zone layer and a stiffer surrounding solid, *J. geophys. Res.,* **107**(B2), 2042, doi:10.1029/2001JB000254.

Ben-Zion, Y. & Malin, P., 1991. San Andreas fault zone head waves near Parkfield, California, *Science,* **251,** 1592–1594.

Ben-Zion, Y. & Sammis, C.G., 2003. Characterization of fault zones, *Pure appl. Geophys.,* **160,** 677–715.

Ben-Zion, Y. & Shi, Z., 2005. Dynamic rupture on a material interface with spontaneous generation of plastic strain in the bulk, *Earth planet. Sci. Lett.,* **236,** 486–496.

Ben-Zion, Y., Katz, S. & Leary, P., 1992. Joint inversion of fault zone head waves and direct P arrivals for crustal structure near major faults, *J. geophys. Res.,* **97,** 1943–1951.

Ben-Zion, Y. *et al*., 2003. Shallow fault zone structure illuminated by trapped waves in the Karadere-Duzce branch of the North Anatolian Fault, western Turkey, *Geophys. J. Int.,* **152,** 699–717.

Ben-Zion, Y., Rockwell, T., Shi, Z. & Xu, S., 2012. Reversed-polarity secondary deformation structures near fault stepovers, *J. Appl. Mech.,* **79,** 031025, doi:10.1115/1.4006154.

Bennington, N.L., Thurber, C.H., Zhang, H., Peng, Z. & Zhao, P., 2011. Incorporating fault zone head wave and direct wave secondary arrival times into seismic tomography: application at Parkfield, California, *EoS Trans. AGU, Fall Mtg. Suppl.,* Abstract T13G-02.

Bleibinhaus, F., Hole, J.A., Ryberg, T. & Fuis, G.S., 2007. Structure of the California Coast Ranges and San Andreas Fault at SAFOD from seismic waveform inversion and reflection imaging, *J. geophys. Res.,* **112,** 6315–6330, doi:10.1029/2006JB004611.

Boness, N.L. & Zoback, M.D., 2006. A multi-scale study of the mechanisms controlling shear velocity anisotropy in the San Andreas Fault Observatory at Depth, *Geophysics,* **71,** F131–F146.

Brietzke, G.B., Cochard, A. & Igel, H., 2009. Importance of biomaterial interfaces for earthquake dynamics and strong ground motion, *Geophys. J. Int.,* **178**(2), 921–938.

Chen, P., Zhao, L. & Jordan, T.H., 2007. Full 3D tomography for the crustal structure of the Los Angeles Region, *Bull. seism. Soc. Am,* **97**(4), 1094–1120.

Cochran, E.S., Vidale, J.E. & Li, Y.-G., 2003. Near-fault anisotropy following the Hector Mine earthquake, *J. geophys. Res.,* **108**(B9), 2436–2447, doi:10.1029/2006JB004611.

DeDontney, N., Rice, J. & Dmowska, R., 2011. Influence of material contrast on fault branching behavior, *Geophys. Res. Lett.,* **38,** 14305–14310, doi:10.1029/2011GL047849.

DeMets, C., 1995. Plate motions and crustal deformation, 1995, U.S. National Report to International Union of Geodesy and Geophysics 1991–1994, *Rev. Geophys.,* **33,** 365–369

DeMets, C. & Dixon, T., 1999. New kinematic models for Pacific-North America motion from 3 Ma to present, 1: evidence for steady motion and biases in the NUVEL-1A model, *Geophys. Res. Lett.,* **26,** 1921–1924.

Dieterich, J.H. & Kilgore, B.D., 1994. Direct observation of frictional contacts: new, insights for state-dependent properties, *Pure appl. Geophys.,* **143,** 283–302.

Doan, M.-L. & Billi, A., 2011. High strain rate damage of Carrara marble, *Geophys. Res. Lett.,* **38,** L19302, doi:10.1029/2011GL049169.

Dor, O., Rockwell, T.K. & Ben-Zion, Y., 2006. Geologic observations of damage asymmetry in the structure of the San Jacinto, San Andreas and Punchbowl faults in southern California: a possible indicator for preferred rupture propagation direction, *Pure appl. Geophys.,* **163,** 301–349, doi:10.1007/s00024-005-0023-9.

Dunham, E.M., Belanger, D., Cong, L. & Kozdon, J.E., 2011. Earthquake ruptures with strongly rate-weakening friction and off-fault plasticity, 2: nonplanar faults, *Bull. seism. Soc. Am.,* **101**(5), 2308–2322.

Eberhart-Phillips, D. & Michael, A., 1993. Three-dimensional velocity structure, seismicity, and fault structure in the Parkfield region, central California, *J. geophys. Res.,* **98,** 15 737–15 758.

Fay, N.P. & Humphreys, E.D., 2005. Fault slip rates, effects of elastic heterogeneity on geodetic data, and the strength of the lower crust in the Salton Trough region, southern California, *J. geophys. Res.,* **110,** B09401, doi:10.1029/2004JB003548.

Fialko, Y., 2004. Probing the mechanical properties of seismically active crust with space geodesy: study of the co-seismic deformation due to the

1992 M_w 7.3 Landers (southern California) earthquake, *J. geophys Res.,* **109,** B03307, doi:10.1029/2003JB002756.

Fialko, Y., 2006. Interseismic strain accumulation and the earthquake potential on the southern San Andreas fault system, *Nature,* **441,** 968–971.

Finzi, Y., Hearn, E.H., Lyakhovsky, V. & Ben-Zion, Y., 2009. Structural properties and deformation patterns of evolving strike-slip faults: numerical simulations incorporating damage rheology, *Pure appl. Geophys.,* **166,** 1537–1573, doi:10.1007/s00024-009-0522-1.

Fishwick, S., Heintz, M., Kennet, B.L.N., Reading, A.M. & Yoshizawa, K., 2008. Steps in lithospheric thickness within eastern australia, evidence from surface wave tomography, *Tectonics,* **27,** TC4009, doi:10.1029/2007TC002116.

Graves, R.W., 2008. The seismic response of the San Bernadino basin region during the 2001 Big Bear Lake earthquake, *Bull. seism. Soc. Am.,* **98,** 241–252.

Hauksson, E., 2000. Crustal structure and seismicity distribution adjacent to the Pacific and North America plate boundary in southern California, *J. geophys. Res.,* **105,** 13 875–13 904.

Hauksson, E., Yang, W. & Shearer, P.M., 2012. Waveform relocated earthquake catalog for Southern California (1981 to 2011), *Bull. seism. Soc. Am.,* (in press).

Helmberger, D.V., Stead, R., Ho-Liu, P. & Dreger, D.S., 1992. Broadband modeling of regional seismograms; Imperial Valley to Pasadena, *Geophys. J. Int.,* **110,** 42–54.

Hong, T.-K. & Menke, W., 2006. Tomographic investigation of the wear along the San Jacinto fault, southern California, *Phys. Earth Planet. In.,* **155,** 236–248.

Hough, S.E., Ben-Zion, Y. & Leary, P., 1994. Fault zone waves observed at the southern Joshua Tree earthquake rupture zone, *Bull. seism. Soc. Am.,* **84,** 761–767.

Jennings, C. (compiler), 1977, Geologic map of California: San Francisco, California Division of Mines and Geology, scale 1:750,00. California Department of Conservation, Division of Mines, Sacramento, CA.

Jennings, S. & Thompson, G.R., 1986. Diagenesis of Plio-Pleistocene sediments of the Colorado River delta, southern California, *J. Sed. Petrol.,* **56,** 89–98.

Johnson, P.A. & Jia, X., 2005. Non-linear dynamics, granular media and dynamic earthquake triggering, *Nature,* **473,** 871–874.

Kendrick, K.J., Morton, D.M., Wells, S.G. & Simpson, R.W., 2002. Spatial and temporal deformation along the northern San Jacinto fault, southern California: implications for slip rates, *Bull. seism. Soc. Am.,* **92**(7), 2782–2802.

Kim, Y.-S., Peacock, D.C.P. & Sanderson, D.J., 2004. Fault damage zones, *J. Struct. Geol.,* **26,** 503–517.

Kirby, S.M., Janecke, S.U., Dorsey, R.J., Housen, B.A., McDougall, K., Langenheim, V. & Steely, A., 2007. Pleistocene Brawley and Ocotillo formations: evidence for initial strike-slip deformation along the San Felipe and San Jacinto fault zones, *Calif. J. Geol.,* **115,** 43–62.

Langenheim, V.E., Jachens, R.C., Morton, D.M., Kistler, R.W. & Matti, J.C., 2004. Geophysical and isotopic mapping of preexisting crustal structures that influenced the location and development of the San Jacinto fault zone, Southern California, *GSA Bull.,* **116**(9–10), 1143–1157.

Lengline, O. & Got, J.-L., 2011. Rupture directivity of micro-earthquake sequences near Parkfield, California, *Geophys. Res. Lett.,* **38,** L08310, doi:10.1029/2011GL047303.

Le Pichon, X., Kreemer, C. & Chamot-Rooke, N., 2005. Asymmetry in elastic properties and the evolution of large continental strike-slip faults, *J. geophys. Res.,* **110,** B03405, doi:10.1029/2004JB003343.

Lévêque, J.J., Rivera, L. & Wittlinger, G., 1993. On the use of checker-board test to assess the resolution of tomographic inversions, *Geophys. J. Int.,* **115,** 313–318.

Lewis, M.A. & Ben-Zion, Y., 2010. Diversity of fault zone damage and trapping structures in the Parkfield section of the San Andreas Fault from comprehensive analysis of near fault seismograms, *Geophys. J. Int.,* **183,** 1579–1595, doi:10.1111/j.1365-246X.2010.04816.x.

Lewis, M.A., Peng, Z., Ben-Zion, Y. & Vernon, F.L., 2005. Shallow seismic trapping structure in the San Jacinto fault zone near Anza, California, *Geophys. J. Int.,* **162,** 867–881, doi:10.1111/j.1365-246X.2005.02684.x.

Lewis, M.A., Ben-Zion, Y. & McGuire, J., 2007. Imaging the deep structure of the San Andreas Fault south of Hollister with joint analysis of fault-zone head and direct P arrivals, *Geophys. J. Int.,* **169,** 1028–1042.

Li, Y.-G. & Vernon, F.L., 2001. Characterization of the San Jacinto fault zone near Anza, California, by fault zone trapped waves, *J. geophys. Res.,* **106,** 30 671–30 688.

Lin, G., Shearer, P.M., Hauksson, E. & Thurber, C.H., 2007. A three-dimensional crustal seismic velocity model for southern California from a composite event method, *J. geophys. Res.,* **112,** B11306, doi:10.1029/2007JB004977.

Lin, G., Thurber, C.H., Zhang, H., Hauksson, E., Shearer, P., Waldhauser, F., Brocher, T.M. & Hardebeck, J., 2010. A California statewide three-dimensional seismic velocity model from both absolute and differential times, *Bull. seism. Soc. Am.,* **100,** 225–240.

Lyakhovsky, V. & Ben-Zion, Y., 2009. Evolving geometrical and material properties of fault zones in a damage rheology model, *Geochem. Geophys. Geosyst.,* **10,** Q11011, doi:10.1029/2009GC002543.

Lyakhovsky, V., Hamiel, Y. & Ben-Zion, Y., 2011. A non-local visco-elastic damage model and dynamic fracturing. *J. Mech. Phys. Solids,* **59,** 1752–1776, doi:10.1016/j.jmps.2011.05.016.

Ma, S. & Andrews, D.J., 2010. Inelastic off-fault response and three-dimensional earthquake rupture dynamics on a strike-slip fault, *J. geophys. Res.,* **115,** B04304, 4304–4320, doi:10.1029/2009JB006382.

Magistrale, H. & Sanders, C., 1995. P wave image of the Peninsular Ranges batholith, southern California, *Geophys. Res. Lett.,* **22,** 2549–2552.

Magistrale, H., Day, S., Clayton, R.W. & Graves R., 2000. The SCEC southern California reference 3D seismic velocity model Version 2, *Bull. seism. Soc. Am.,* **90**(6B), S65–S76.

McGuire, J. & Ben-Zion, Y., 2005. High-resolution imaging of the Bear Valley section of the San Andreas Fault at seismogenic depths with fault-zone head waves and relocated seismicity, *Geophys. J. Int.,* **163,** 152–164, doi:10.1111/j.1365-246X.2005.02703.x.

McNally, K.C. & McEvilly, T.V., 1977. Velocity contrast across the San Andreas fault in central California: small-scale variations from P-wave nodal plane distortion, *Bull. seism. Soc. Am.,* **67,** 1565–1576.

Michael, A.J. & Eberhart-Phillips, D.M., 1991. Relations among fault behavior, subsurface geology, and three-dimensional velocity models, *Science,* **253,** 651–654.

Morton, N., Girty, G.H. & Rockwell, T.K., 2012. Fault zone architecture of the San Jacinto fault zone in Horse Canyon, southern California: a model for focused post-seismic fluid flow and heat transfer in the shallow crust, *Earth planet. Sci. Lett.,* **330,** 71–83, doi:10.1016/j.espl.2012.02.013

Oppenheimer, D.H., Reasenberg, P.A. & Simpson, R.W., 1988. Fault plane solutions for the 1984 Morgan Hill, California, earthquake sequence: evidence for the state of stress on the Calaveras fault, *J. geophys. Res.,* **93,** 9007–9026.

Paige, C.C. & Saunders, M.A., 1982. LSQR: sparse linear equations and least squares problems, *ACM Trans. Math. Softw.,* **8,** 195–209.

Peng, Z. & Ben-Zion, Y., 2004. Systematic analysis of crustal anisotropy along the Karadere-Duzce branch of the north Anatolian fault, *Geophys. J. Int.,* **159,** 253–274, doi:10.1111/j.1365-246X.2004.02379.x.

Peng, Z., Ben-Zion, Y., Michael, A.J. & Zhu, L., 2003. Quantitative analysis of seismic trapped waves in the rupture zone of the 1992 Landers, California earthquake: evidence for a shallow trapping structure, *Geophys. J. Int.,* **155,** 1021–1041.

Plesch, A., Tape, C., Graves, J.R., Small, P., Ely, G. & Shaw, J.H., 2011. Updates for the CVM-H including new representations of the offshore Santa Maria and San Bernardino basin and a new Moho surface, in *2011 SCEC Annual Meeting, Proceedings and Abstracts,* Vol. 21, B128, Southern California Earthquake Center, Los Angeles, CA.

Richards-Dinger, K.B. & Shearer, P.M., 2000. Earthquake locations in Southern California obtained using source-specific station terms, *J. geophys. Res.,* **105,** 10 939–10 960.

Rockwell, T., Loughman, C. & Merifield, P., 1990. Late Quaternary rate of slip along the San Jacinto fault zone near Anza, Southern California, *J. geophys. Res. B,* **95**(6), 8593–8605.

Rockwell, T.K. & Seitz, G.G., 2008. Observations of mode-switching from long paleoseismic records of earthquakes on the San Jacinto and San Andreas faults: implications for making hazard estimates from short paleoseismic records, in *33rd International Geological Congress,* Oslo, Norway.

Rockwell, T.K., *et al.*, 2003. 3,000 years of ground-rupturing earthquakes in the Anza Seismic Gap, San Jacinto fault, souther California: time to shake it up?, *Seismol. Res. Lett.,* **74,** 236–237.

Rockwell, T.K., Seitz, G.G., Dawson, T.E. & Young, J., 2006. The long record of San Jacinto Fault paleoearthquakes at Hog Lake; implications for regional patterns of strain release in the southern San Andreas Fault system, *Seismol. Res. Lett.,* **77,** 270–296.

Roux, P., Wathelet, M. & Roueff, A., 2011. The San Andreas Fault revisited through seismic-noise and surface-wave tomography, *Geophys. Res. Lett.,* **38,** L13319, doi:10.1029/2011GL047811.

Rovelli, A., Caserta, A., Marra, F. & Ruggiero, V., 2002. Can seismic waves be trapped inside an inactive fault zone? The case study of Nocera Umbra, Central Italy, *Bull. seism. Soc. Am.,* **92,** 2217–2232.

Rubin, A. & Gillard, D., 2000. Aftershock asymmetry/rupture directivity among central San Andreas fault microearthquakes, *J. geophys. Res.,* **105**(B8), 19 095–19 109.

Salisbury, J.B., Rockwell, T.K., Middleton, T.J. & Hudnut, K.W., 2011. LiDAR and field observations of slip distribution for the most recent surface ruptures along the central San Jacinto Fault, *Bull. seism. Soc. Am.,* **102,** 598–619, doi:10.1785/0120110068.

Scott, J.S., Masters, T.G. & Vernon, F.L., 1994. 3-D velocity structure of the San Jacinto fault zone near Anza, California–I. P waves, *Geophy. J. Int.,* **119,** 611–626.

Shapiro, N.M., Campillo, M., Stehly, L. & Ritzwoller, M.H., 2005. High resolution surface-wave tomography from ambient seismic noise, *Science,* **29,** 1615–1617.

Sharp, R.V., 1967. San Jacinto fault zone in the Peninsular Ranges of southern California, *Geol. Soc. Am. Bull.,* **78,** 705–730.

Shi, Z. & Ben-Zion, Y., 2006. Dynamic rupture on a bimaterial interface governed by slip-weakening friction, *Geophys. J. Int.,* **165,** 469–484.

Silver, L.T. & Chappell, B.W., 1988. The Peninsular Ranges Batholith: an insight into the evolution of the Cordilleran batholiths of southwestern North America, *Trans. R. Soc. Edinburgh Earth Sci.,* **79,** 105–121.

Stierman, D.J., 1984. Geophysical and geological evidence for fracturing, water circulation, and chemical alteration in granitic rocks adjacent to major strike-slip faults, *J. geophys. Res.,* **89,** 5849–4857.

Süss, M.P. & Shaw, J.H., 2003. P-wave seismic velocity structure derived from sonic logs and industry reflection data in the Los Angeles basin, California, *J. geophys. Res.,* **108,** 2170–2181.

Tape, C., Liu, Q., Maggi, A. & Tromp, J., 2009. Adjoint tomography of the southern California crust, *Science,* **325,** 988–992.

Tape, C., Liu, Q., Maggi, A. & Tromp, J., 2010. Seismic tomography of the southern California crust based on spectral-element and adjoint methods, *Geophys. J. Int.,* **180,** 433–462.

Thurber, C.H. & Eberhart-Phillips, D., 1999. Local earthquake tomography with flexible gridding, *Comput. Geosci.,* **25,** 809–818.

Thurber, C., Zhang, H., Waldhauser, F., Hardebeck, J., Micheal, A. & Eberhart-Phillips, D., 2006. Three-dimensional compressional wavespeed model, earthquake relocations, and focal mechanisms for the Parkfield, California, region, *Bull. seism. Soc. Am.,* **96**(4B), S38–S49.

Unsworth, M., Egbert, G. & Booker, J., 1999. High-resolution electromagnetic imaging of the San Andreas Fault in Central California, *J. geophys. Res.,* **104,** 1131–1150.

Waldhauser, F. & Ellsworth, W.L., 2000. A double-difference earthquake location algorithm: method and application to the Northern Hayward Fault, California, *Bull. seism. Soc. Am.,* **90**(6), 1353–1368.

Wdowinski, S., Smith, B., Bock, Y. & Sandwell, D., 2007. Diffuse intersesimic deformation across the Pacific-North America plate boundary, *Geology,* **35,** 311–314.

Wechsler, N., Rockwell, T.K. & Ben-Zion, Y., 2009. Analysis of rock damage asymmetry from geomorphic signals along the trifurcation area of the San-Jacinto Fault, *Geomorphology,* **113,** 82–96.

Weertman, J., 1980. Unstable slippage across a fault that separates elastic media of different elastic constants, *J. geophys. Res.,* **85,** 1455–1461.

Yang, H. & Zhu, L., 2010. Shallow low-velocity zone of the San Jacinto fault from local earthquake waveform modelling, *Geophys. J. Int.,* **183,** 421–432.

Yang, H., Zhu, L. & Cochran, E., 2011. Seismic structures of the Calico fault zone inferred from local earthquake travel time modeling, *Geophys. J. Int.,* **186,** 760–770.

Zaliapin, I. & Ben-Zion, Y., 2011. Asymmetric distribution of aftershocks on large faults in California, *Geophys. J. Int.,* **185,** 1288–1304.

Zhang, H. & Thurber, C.H., 2003. Double-difference tomography: the method and its application to the Hayward fault, California, *Bull. seism. Soc. Am.,* **93,** 1875–1889.

Zhang, H., Thurber, C.H., Shelly, D., Ide, S., Beroza, G.C. & Hasegawa, A., 2004. High-resolution subducting-slab structure beneath northern Honshu, Japan, revealed by double-difference tomography, *Geology,* **32**(4), 361–364.

Zhao, P. & Peng, Z., 2009. Depth extent of damage zones around the central Calaveras fault from waveform analysis of repeating earthquakes, *Geophys. J. Int.,* **179,** 1817–1930.

Zhao, P., Peng, Z., Shi, Z., Lewis, M. & Ben-Zion, Y., 2010. Variations of the velocity contrast and rupture properties of M6 earthquakes along the Parkfield section of the San Andreas Fault, *Geophys. J. Int.,* **180,** 765–780, doi:10.1111/j.1365-246X.2009.04436.x.

APPENDIX A: INVERSION PARAMETERS AND RESOLUTION ANALYSIS

In addition to the coverage provided by the available earthquakes and recording stations, the inversion results are affected by a number of algorithmic parameters. The most important of these is a 'smoothing' parameter that controls the amplitude of the spatial variations of seismic velocities. If smoothing is too low, the inversion is allowed to perturb adjacent velocities to unrealistic values, creating small-scale fluctuations with steep gradients that deflect propagating rays. After the first iteration, when the model has the most freedom to change, such gradients come to dominate the ray tracing portion of successive iterations. The end result is an implausible 'blobby' velocity model with an almost random distribution of high- and low-velocity zones. If smoothing is too high, the inversion is inhibited from creating velocity structures which may exist in reality. For example, near-fault low-velocity zones can be completely smoothed away. Because fault zone features are of particular interest in this study, they should ideally be reflected in the final model. Thus, smoothing should be set by trial-and-error just high enough to prevent unrealistic fluctuations to ray paths, but low enough to produce resolvable physical structures.

Another algorithmic parameter is a 'damping' parameter. Damping limits the magnitude of the perturbation to the model in a single iteration. This is important because of the non-linearity of the problem, which comes mainly from two sources: the dependence of the ray paths and hypocentre locations on the model structure. If the velocity structure is perturbed too much in a single iteration, the assumption of cancelling ray paths in eq. (4) becomes invalid. However, too much damping leads to a model that reflects a local minimum of the misfit function. In practice, we find that the damping has little impact on the resulting velocity model; the inversion does not get 'trapped' in local minima even for high-damping values. As such, we use the DDT default damping of 70. Other inversion parameters, including the grid spacing, number of iterations and data set weighting are discussed in Section 2.2.

A common method for assessing the resolution of tomographic models is the so-called 'checkerboard' test. This method is gener-

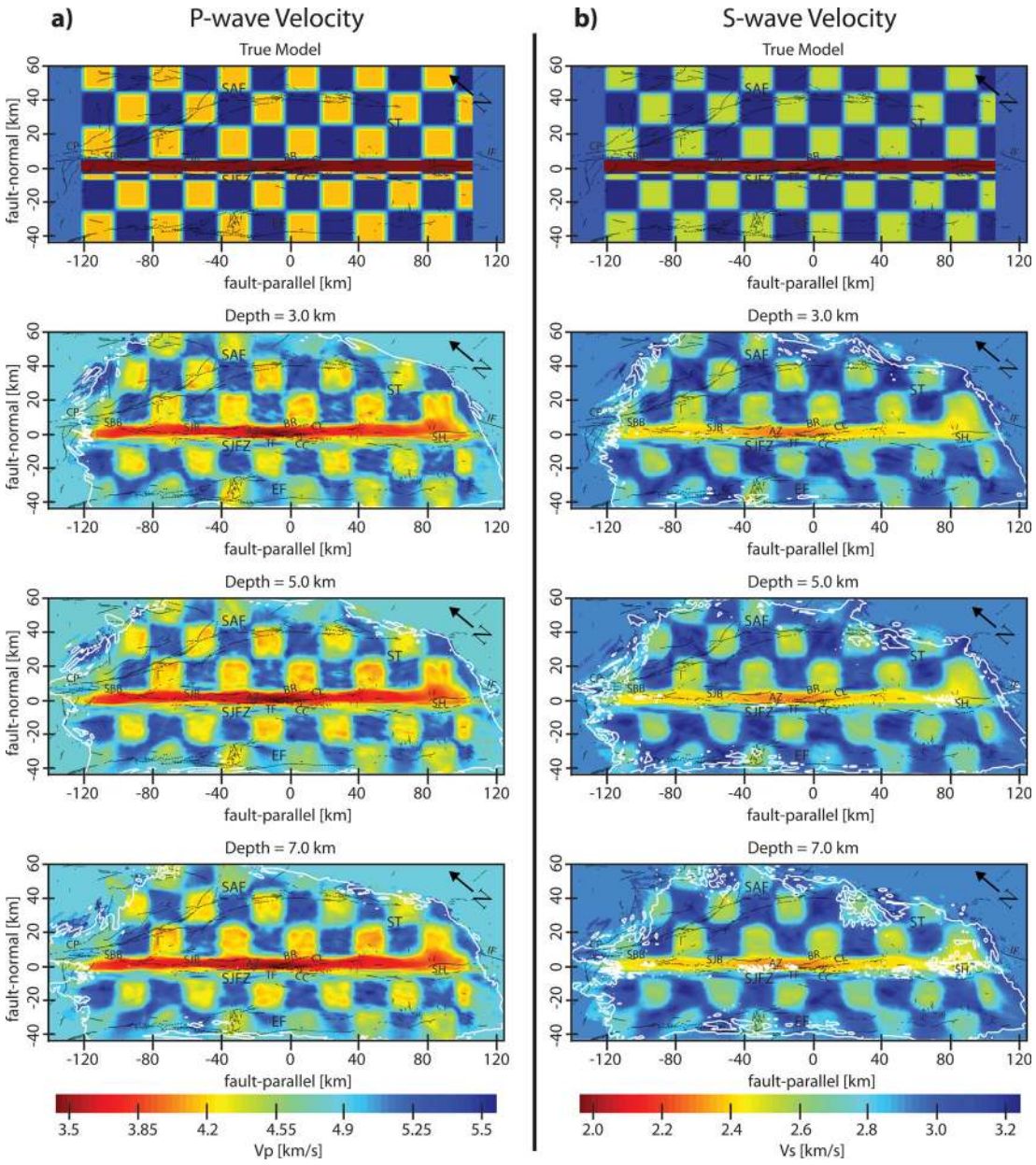

Figure A1. Map views at different depths of synthetic models for (a) V_p and (b) V_s. The initial model (top) is a vertical low-velocity zone embedded in a 20 km checkerboard; there is no variation with depth. Recovery is good, especially near the Anza and trifurcation segments of the SJFZ. V_p recovery is generally better than V_s because of the higher number of *P*-wave traveltime picks employed in the inversion.

ally applied to large-scale mantle tomography, where the targeted velocity anomalies are large with respect to the total grid size and roughly equidimensional (e.g. Fishwick *et al.* 2008). As the structure around a fault zone is expected to be narrower in the fault-perpendicular direction and more extensive in the fault-parallel direction and with depth, we employ both classical checkerboard tests as well as tests modified to mimic potential fault zone structure. We present one such test here (Fig. A1) and more in the Supporting Information.

First, we construct the starting model shown in Fig. A1 (top). This model includes a through-going low-velocity fault zone extending to the bottom of the model, similar to the 'vertical sandwich' of Zhang & Thurber (2003), combined with checkerboard features with dimensions of 20 grid points in both the x and y directions. Because the grid spacing is variable in the y directions, near-fault checkers are distorted. The *P*-wave velocity is a constant 1.732 times the *S*-wave velocity, a value corresponding to a Poisson Solid. Secondly, we compute the complete *P* and *S* wave traveltime catalogue for this model using the built-in ray tracing software of TomoDD (Thurber & Eberhart-Phillips 1999) and the real earthquake and receiver locations shown in Fig. 1. Finally, we treat this catalogue as the 'true' data set, and we perform a double-difference inversion using the parameters described in Section 2.2 from a homogeneous starting model.

Fig. A1(a) demonstrates how well the assumed 'true' structure is recovered from the real source–receiver geometry at various depths for *P*-wave velocity. Fig. A1(b) shows the results for *S*-wave velocity. In general, both the checkerboard and the low-velocity fault zone layer are well resolved, and sharp velocity contrasts are recovered along the various assumed interfaces. The results

demonstrate the ability of the employed methods and data set to recover fault zone velocity structures variable in both size and interface contrast. Though the traveltimes in the performed test are not sensitive strictly to the same portions as in the actual crust, these results nevertheless support the validity of the images presented in Figs 4–9. In particular, we note that we could have recovered a continuous low-velocity fault zone layer that extends to the bottom of the seismogenic zone if such was a feature of the SJFZ.

Though the results show good recovery for both the *P* and *S* velocity structure, the *P* wave recovery is in general higher resolution and features sharper velocity contrasts. Because of this, computation of V_p/V_s ratios leads to very noisy images which are difficult to interpret. In the Supporting Information, we present V_p/V_s images for both the final velocity model and for the synthetic model shown in Fig. A1. Comparison of these images provides some confidence that large-scale persistent features of the final V_p/V_s model are features present in the real Earth.

APPENDIX B: GRID SPACING

We perform our inversions in a discretized model space of dimensions 270 × 105 × 35 km in a coordinate system rotated 40° counterclockwise to approximately fault-parallel (*x*) and fault-normal (*y*) axes. The origin of the rotated coordinate system is placed at 33.5° N latitude and 116.5° W longitude. The grid cells in the *x* and *z* (depth) directions are uniformly spaced at 1 km. In the *y* direction, the grid spacing varies as follows (grid coordinates are in units of km): 1 km from −45 to −10, 500 m from −9.5 to −8, 200 m from −7.8 to −5, 100 m from −4.9 to −0.1, 200 m from 0 to 1.8, 500 m from 2 to 4.5 and 1 km from 5 to 60. Boundary nodes are placed at −300 and 300 km in both the *y* and *x* directions to produce a buffer zone around the region of interest. Geographical location of the nodes in latitude and longitude are shown in Fig. S1 of the Supporting Information. The following MATLAB code fragment summarizes the node locations:

```
x = [-300  -143:dx:125  300]

y = [-300  -45:-10  -9.5:.5:-8  -7.8:.2:-5
     -4.9:.1:-0.1  0:.2:1.8  2:.5:4.5  5:60  300]

z = [-1.5  0:35  300]
```

SUPPORTING INFORMATION

Additional Supporting Information may be found in the online version of this article:

Figure S1. Location map for the grid points used in the inversion. The grid nodes in the fault-parallel (*x*) and depth (*z*) directions are uniformly spaced at 1 km, while a variable grid is employed in the fault-normal (*y*) direction. The grid spacing is reduced near the SJFZ; this is supported by high derivate weight sum (DWS) values near the fault.

Figure S2. Map views at different depths for two different synthetic models of V_p: (a) a 15 km checkerboard and (b) a 500 m fault zone. The initial 'True' models (top) do not vary with depth. For (a), the checks are recovered with a minimum of streaking across all depths shown, with some distortions near the edges of the imaged region. For (b), a 500 m low-velocity zone is recovered, though it is broadened and the amplitude of the velocity reduction is decreased. Nevertheless, this demonstrates the ability of the current parametrization to capture even very small-scale fault zone features.

Figure S3. Map views at different depths for the V_p/V_s ratio of the models shown in Fig. A1. Both the V_p and V_s initial models are vertical low-velocity zones embedded in a 20 km checkerboard; there is a constant V_p/V_s ratio of 1.73 in the initial model (top). Though the two models are well imaged separately (Figs A1a and b), the different resolutions lead to numerical noise when V_p/V_s is calculated.

Figure S4. Similar to Figs 4 and 5 for values of the velocity ratio V_p/V_s. A value of 1.732 corresponds to a Poisson solid. High ratios are observed along the central SJFZ, in the San Bernardino and San Jacinto basins and below the Salton Trough. Low ratios are prominent in the Salton Trough and in patchy areas around the major faults. Comparison of this result to the V_p/V_s ratios of the synthetic model shown in Fig. S3 yields some confidence in the interpretation of the large-scale persistent features.

Figure S5. Similar to Figs 6 and 7 for values of the velocity ratio V_p/V_s. Low ratios are observed in profiles 1–6 along the SJFZ. The highly patchy character of the images may reflect heterogeneities as well as variable resolution.

Please note: Wiley-Blackwell are not responsible for the content or functionality of any supporting materials supplied by the authors. Any queries (other than missing material) should be directed to the corresponding author for the article.